Study on the seasonal variation of Aeolus detection performance over China using ERA5 and radiosonde data

Siying Chen[1], Rongzheng Cao[1], Yixuan Xie[1], Yinchao Zhang[1*], Wangshu Tan[1], He Chen[1], Pan Guo[1], and Peitao Zhao[2*]

[1]School of Optics and Photonics, Beijing Institute of Technology, Beijing 100081, China
[2]Meterological Observation Center of CMA, Beijing 100081, China

Correspondence to: Yinchao Zhang (ychang@bit.edu.cn) and Peitao Zhao (peitaozhao@163.com)

Abstract. Aeolus wind products have been available to ordinary users on May 12, 2020. In this paper, the Aeolus wind observations, L-band radiosonde (L-band RS) data and the European Centre for Medium-Range Weather Forecasts (ECMWF) fifth generation atmospheric reanalyses (ERA5) are used to analyse the seasonality of Aeolus detection performance over China. Based on the Rayleigh-clear data and Mie-cloudy data, the data quality of the Aeolus effective detection data is verified, and the results show that the Aeolus data is in good agreement with the L-band RS data and the ERA5 data. The relative errors of Aeolus data in the four regions (Chifeng, Baoshan, Shapingba and Qingyuan) in China were calculated according to different months (July to December 2019, May to October 2020). The relative error of the Rayleigh-clear data in summer is significantly higher than that in winter, as the mean relative error parameter in July is 174% higher than that in December. Besides, the distribution about the wind direction and the high-altitude clouds in different months (July and December) are analysed. The results show that the distribution of angle, between the horizontal wind direction of the atmosphere and the horizontal line of sight (HLOS), has a greater proportion in the high error interval (70 °–110 °) in summer, and this proportion is 8.14% higher in July than in December. In addition, the cloud top height in summer is about 3–5km higher than in winter, which may reduce the signal-to-noise ratio (SNR) of Aeolus. The results show that the detection performance of Aeolus is affected by seasonal factors, which may be caused by seasonal changes in wind direction and cloud distribution.

1 Introduction

Global wind field data are indispensable meteorological parameters in weather forecasting (Ishii et al., 2017). To this end, the European Space Agency (ESA) proposed the Atmospheric Dynamics Mission Aeolus (ADM-Aeolus) in 1999. Aeolus is equipped with a 355nm direct-detection wind lidar, which uses a single-view detection method to scan the global three-dimensional wind field from space. In addition, it adopts a dual-channel design and uses different frequency discriminators to receive the Mie channel and Rayleigh channel signals respectively (Stoffelen et al., 2005; Reitebuch, 2012). Aeolus was successfully launched on 22 August 2018, becoming the world's first spaceborne wind lidar in orbit. Then, it sent back the first batch of wind profile data, proving that the satellite-borne direct-detection wind lidar has the ability to provide global wind profiles (Reitebuch et al., 2019). On 12 May 2020, ESA opened Aeolus' wind measurement products to the public (https://earth.esa.int/eogateway/news/aeolus-data-now-publicly-available, last access: 13 March 2021), including Level 1B and 2B products. Among them, Level 2B products provide HLOS wind data after actual atmospheric correction and deviation correction (European Space Agency et al., 2008), which are used in this paper.

In order to accurately calibrate the Doppler lidar carried on Aeolus, relevant researchers have carried out a series of verification and comparison studies on Aeolus' wind products. After the launch of Aeolus, the special verification work for Aeolus was carried out immediately. The main verification methods included radiosonde (Baars et al., 2020) and airborne lidar (Witschas et al., 2020; Lux et al., 2020), in which Aeolus' airborne prototype ALADIN (Atmospheric Laser Doppler Instrument) Airborne Demonstrator (A2D) was also used. In the following two years, researchers around the world completed regional verification of the Aeolus detection data using a variety of detection means, including satellites (Shin et al., 2020), ground-based lidar

40 (Hauchecorne et al., 2020), ground-based wind profiler radar (Belova et al., 2021; Guo et al., 2021), and radiosonde (Liu et al., 2021). In addition, global Aeolus data verification work using the NWP model has also been carried out (Martin et al., 2021; Rennie and Isaksen, 2019) . These verifications not only deepened our understanding of Aeolus data quality, but also discovered some factors that affect Aeolus data quality during the verification process, such as solar background radiation (Zhang et al., 2020), satellite flight direction (Guo et al., 2021), seasonal changes (Martin et al., 2021), etc. ECWMF also

45 revised the data processing algorithm in time, such as the temperature gradient correction algorithm for M1, which is the main mirror of the Aeolus telescope, to solve the problem of seasonal changes (Rennie and Isaksen, 2019).

So far, very few studies on the seasonal fluctuation of Aeolus detection performance over China have been reported, especially using actual detection data. After the implementation of the new M1 deviation correction scheme, the effect of system thermal performance changes on Aeolus' seasonal fluctuation is theoretically excluded. However, the actual atmospheric conditions

50 in different seasons tend to affect the detection performance of lidar.

In this paper, the variation of Aeolus detection performance in different seasons is analysed by using Aeolus L2B wind products in four regions of China from 12 months (July to December 2019, May to October 2020), compared with the L-band RS detection data and the ERA5 reanalysis data. Two conjectures about Aeolus different detection capabilities are introduced and verified.

55 2 Data and methods

In order to compromise the consistency of meteorological conditions and the abundance of detection data, the Aeolus L2B data are compared with ERA5 data and the L-band RS detection data, within ±2.5° (latitude and longitude) geographical range (Fig. 1) near the target L-band RS station. The four L-band RS stations in Fig. 1 are selected because they have obvious differences in geographic location and meteorological conditions.

60

Figure 1. The geographic location of the L-band RS site and the Aeolus measurement trajectory.   In the partial enlarged view (http://aeolus-ds.eo.esa.int/socat/L1B_L2_Products), the red rectangles represent the range of ±2.5° around the L-band RS stations, and the gray-green lines represent Aeolus' overlapping trajectories of the 12 months.

2.1 Aeolus L2B wind products

65 A sun-synchronous dawn-dusk orbit with a height of about 320 km is selected by Aeolus, and the orbit repeats its ground track every seven days (European Space Agency et al., 2008). The transit time of Aeolus over the central and eastern China is

generally around 10:00 UTC and 22:00 UTC. In this paper, the criterion for judging the validity of Aeolus data are the validity flags (0=invalid and 1=valid) and the estimated errors (meet threshold requirements), which can be obtained from Level 2B data. According to ECMWF's recommendations (Rennie and Isaksen, 2020) and the actual situation of the data used in this paper (Fig. 2), the thresholds of estimated errors are 8m/s (Rayleigh-clear) and 4m/s (Mie-cloudy). In this study, the Mie-clear and Rayleigh-cloudy data are discarded because the remaining valid data points of them are too few.
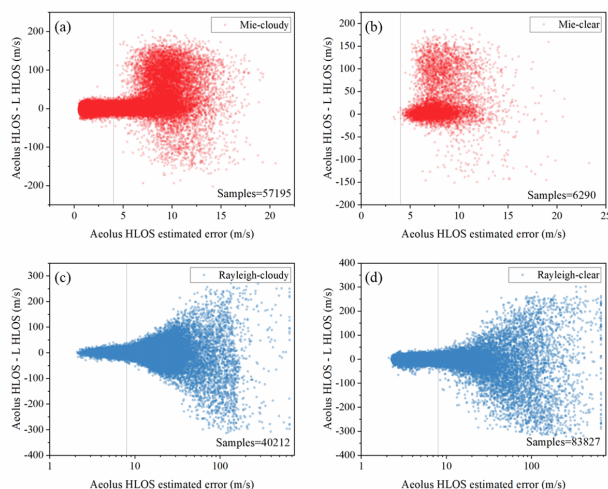
Figure 2. Difference between the Aeolus HLOS and L HLOS wind components as a function of estimated errors for (a) Mie-cloudy, (b) Mie-clear, (c) Rayleigh-cloudy and (d) Rayleigh-clear. Samples mean the number of data points. Reference lines are the screening threshold of estimated errors: 4 m/s (Mie) and 8 m/s (Rayleigh).

2.2 L-band Radiosonde wind data

The L-band radiosonde (L-band RS) is widly used to obtain the true situation of the atmospheric environment, and its detection altitude reach 30km (Guo et al., 2016). In this paper, we use the valid data (the absolute value of wind speed is less than 100 m/s) detected by the four L-band RS stations. Matching of geographic location and time needs attention in the use of L-band lidar. For geographic location, most of the valid L-band RS detection data used in this study have a balloon drift less than 0.5 ° (longitude or latitude). Only a few data points in winter have a maximum balloon drift about 1.6 °. As for the time, the detection time of the L-band RS network in China is 0:00 UTC and 12:00 UTC. Generally, the time of launching the ball is about 45 minutes earlier than the detection time, which is 1 to 2 hours away from the transit time of Aeolus. In order to reduce the impact of time and geographic location differences on this study, ERA5 data are used as reference data.

2.3 ERA5 data

The reanalysis data set is often used as a reference in meteorological data analysis (Hersbach et al., 2020). ERA5 data provided by ECMWF are used in this paper as reference data. It should be noted that the current observation data set used for ERA5 assimilation does not contain the observation results of Aeolus (https://confluence.ecmwf.int/display/CKB/ERA5%3A +data+documentation#ERA5:datadocumentation-TheIFSanddata_assimilation/, last access: 13 March 2021), so there is no mutual influence between the Level 2B data of Aeolus and the reanalysis data of ERA5. In addition to the zonal wind vector u and the meridional wind vector v, the cloud coverage provided in ERA5 is also used in this paper (Sect. 3.2.2). Due to the high resolution of ERA5 in terms of time and geographic location, after matching well with Aeolus data, the difference between ERA5 and L-band RS data is used to represent the wind difference between Aeolus and L-band RS due to time and geographic differences to a certain extent.

2.4 Data matching

Since the L2B data is the final result of Aeolus's single-component wind measurements, it is necessary to decompose the L-band RS and ERA5 data in the direction of Aeolus HLOS. Aeolus has different azimuths at different locations and distances which have been given in the L2B level data. RS data and ERA5 data are decomposed in the HLOS direction:

$$V_{HLOS} = V_{L/ERA5} \times \cos(\theta_{HLOS} - \theta_{L/ERA5}), \tag{1}$$

where $V_{L/ERA5}$ represents the total horizontal wind speed value provided by L-band RS data or ERA5 data. $\theta_{L/ERA5}$ represents the wind direction of the total horizontal wind vector. θ_{HLOS} is the azimuth of Aeolus.

For time matching, both L-band RS and ERA5 take the latest detection data from Aeolus transit the target area ($\pm 2.5°$ near the L-band RS station). For geographic location matching, the selection of the L-band RS station has been determined. The Aeolus data selects the detection data within a ± 2.5 ° (latitude and longitude) rectangular area centered on the L-band RS station (the red rectangular area in Fig.1). For ERA5 data, the data point closest to the latitude and longitude of the Aeolus data are selected. In the vertical direction, due to the difference in the vertical resolution of the three data, both L-band RS data and ERA5 data are matched with the Aeolus data through linear interpolation. For each Aeolus valid data point, L-band RS (ERA5) data points which are just higher and just lower than the Aeolus valid data point are found. We mark them as $V(H^+)$ and $V(H^-)$ and then do a linear interpolation:

$$V_H = \frac{H_{Aeolus} - H^-}{H^+ - H^-} \cdot \left(V(H^+) - V(H^-) \right), \tag{2}$$

where V_H is the L-band RS (ERA5) wind matched with Aeolus data in altitude, and H_{Aeolus} is the altitude of the Aeolus data point.

2.5 Calculation of relative error

Generally, the calculation formula of wind speed error for wind measurement system is:

$$D = V - V_{ture}, \tag{3}$$

where V represents the detection value, and V_{ture} represents the true value of the calibration. This equation is used to calculate the difference between different wind field data. Then for a data set with a sample size of n, its statistical mean error (MD) and standard deviation (SD) are:

$$MD = \frac{1}{n}\sum_{i=1}^{n} D(i), \tag{4}$$

$$SD = \sqrt{\frac{1}{n-1}\sum_{i=1}^{n}(D(i) - MD)^2}, \tag{5}$$

However, because the detection error of Doppler wind lidar tend to increase with the increase of the detected wind speed (Frehlich, 2001), the relative error can better reflect the detection performance of the instrument than the error value. The calculation of relative error is generally as shown in Eq. (6):

$$D_r = \frac{V - V_{ture}}{V_{ture}}, \tag{6}$$

where V_{ture} take the data which have smaller error in the two data. In this paper, it is defaulted that the error of ERA5 data is the smallest while the error of Aeolus data is the largest.

Similarly, for a data set with a sample size of n, the statistical average relative error is:

$$\overline{D}_r = \frac{1}{n}\sum_{i=1}^{n} |D_r(i)|, \tag{7}$$

In the data comparison logic of this paper, both $\overline{D}_r(Aeolus\&L) - \overline{D}_r(L\&ERA5)$ and $\overline{D}_r(Aeolus\&ERA5)$ are used to

130 approximate the relative error value of the Aeolus data when the space-time matching is well. An Aeolus relative error

parameter is set here:

$$D_{Aeolus} = \frac{[\overline{D}_r(Aeolus\&L) - \overline{D}_r(L\&ERA5)] + \overline{D}_r(Aeolus\&ERA5)}{2}, \tag{8}$$

The average value of the comparisons between Aeolus and the two data is used to reduce the possibility of large deviations in

the relative error. D_{Aeolus} is used to approximate the relative error value of the Aeolus data in this paper.

135 **3 Results and discussion**

3.1 quality of data

The comparison results of the three data sources after data matching are shown in Fig. 3. The red and blue points in the figure

represent the data points of the Mie-cloudy and Rayleigh-clear groups respectively. The red and blue lines respectively

represent the linear fitting lines of the data points of the two groups. The Mie-cloudy and Rayleigh-clear groups in the four

140 regions provided 38,275 and 73,131 valid data points in 12 months (July-December 2019, May-October 2020).
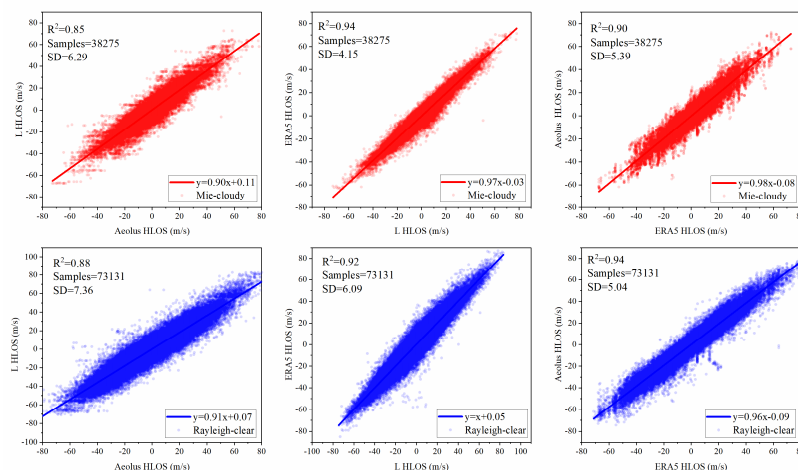
Figure 3. Comparison results of Aeolus data, L-band RS data and ERA5 data in Mie-cloudy and Rayleigh-clear groups. (a,d) Aeolus vs L-band RS, (b,e) L-band RS vs ERA5 and (c,f) ERA5 vs Aeolus.

	Aeolus vs L		L vs ERA5		ERA5 vs Aeolus	
	Mie-cloudy	Rayleigh-clear	Mie-cloudy	Rayleigh-clear	Mie-cloudy	Rayleigh-clear
R	0.92	0.94	0.97	0.96	0.95	0.97
N samples	38275	73131	38275	73131	38275	73131
Slop	0.90	0.91	0.97	1.00	0.98	0.96
Intercept(m/s)	0.11	0.07	-0.03	0.05	-0.08	-0.09
MD(m/s)	-0.04	-0.02	0.24	0.34	0.05	0.05
SD(m/s)	6.29	7.36	4.15	6.09	5.39	5.04

145 **Table 1. Comparison between Aeolus, L HLOS and ERA5 HLOS wind**

Table 1 shows the comparison results of the three groups of data. The consistency of the L-band RS and Aeolus data is the

lower among the three groups for both the Mie-cloudy group and the Rayleigh-clear group. Moreover, the performance of R

value and SD value of this group (Aeolus vs L) is also slightly worse than that of the other two groups, which is in line with

the expectations of this paper. However, there is no significant difference between the comparison results of L-band RS and

150 ERA5 and the comparison results of Aeolus and ERA5. This situation not only shows that the Aeolus and ERA5 data are in

good agreement, but also that the error caused by the space-time matching problem of the L-band RS data may be larger than

expected. But on the whole, the correlation coefficients in the three sets of comparison results are all higher than 0.92, reflecting the reliability of the data used in this paper.

Since this study also involves wind field data in different regions, the impact of geographic location and climate factors on
155   data quality also need be showed. Figure 4 shows the comparison of Aeolus data and L-band RS data in the four regions used in this paper. The blue data points represent the data of the Rayleigh-clear group, and the red data points represent the data of the Mie-cloudy group. The colors of the linear fitting line and related parameters are consistent with the corresponding data points. Table 2 summarizes the comparison results. The consistency of Aeolus and L-band RS data in Qingyuan area is worse than that of the other three groups. This may be due to the fact that Qingyuan is close to the tropics, where the atmospheric
160   convection is active. In addition, from the perspective of the correlation coefficient R, the correlation of the Rayleigh-clear group between the Aeolus data and the L-band RS data is higher, but the SD value is also relatively higher than Mie-cloudy group, which means that the data points are more scattered. As the latitude decreases, the data quality tends to decline, but the data quality of Baoshan is similar to that of Chifeng, which means that this trend is not obvious enough.
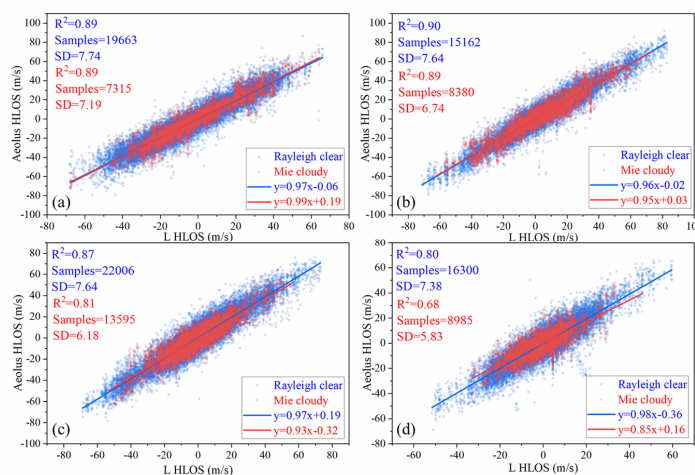
165   **Figure 4. Comparison of Aeolus detection data and L radar detection data in four regions.   The blue data points are the Rayleigh-clear group data, and the red data points are the Mie-cloudy group data. (a) Chifeng, (b) Baoshan, (c) Shapingba, (d) Qingyuan.**

	Chifeng		Baoshan		Shapingba		Qingyuan	
	Mie-cloudy	Rayleigh-clear	Mie-cloudy	Rayleigh-clear	Mie-cloudy	Rayleigh-clear	Mie-cloudy	Rayleigh-clear
R	0.94	0.94	0.94	0.95	0.90	0.93	0.82	0.89
N samples	7315	19663	8380	15162	13595	22006	8985	16300
Slop	0.99	0.97	0.95	0.96	0.93	0.97	0.85	0.98
Intercept(m/s)	0.19	-0.06	0.03	-0.02	-0.32	0.19	0.16	-0.36
MD(m/s)	0.20	0.19	-0.19	-0.21	-0.30	0.20	0.28	-0.37
SD(m/s)	7.19	7.74	6.74	7.64	6.18	7.64	5.83	7.38

Table 2. Comparison results of Aeolus and L-band RS in different regions.

3.2 Seasonal variations in relative errors

After the data quality has been confirmed, the three wind field data are brought into the Eq. (3)-(8) introduced in Section 2 to
170   acquire the errors. The representative statistical distribution of errors is shown in Fig. 5a, which conforms to the Gaussian distribution law.

However, the value of relative error is affected by the denominator in Eq. (6). When the value of the denominator is close to 0, the relative error has a larger outlier. The occurrence of such outlier is sporadic and random, as shown in Fig. 5b. Although most of the relative errors are distributed in the interval [0,3], there are still sporadic outliers in the range greater than 3. These
175   outliers will affect subsequent calculations and must be filtered. The threshold screening method is selected to filter them and

the relative error which is greater than 3 (that is, 300%) is considered as an invalid value. This threshold is derived from the statistical distribution of the relative errors in the all four regions.
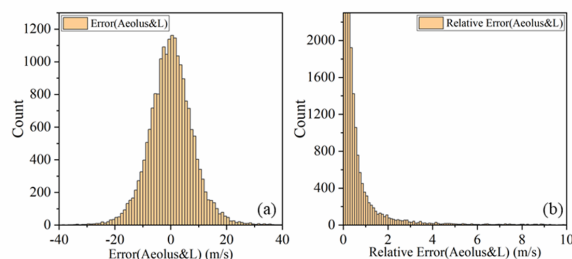
Figure 5. The statistical distribution of the error (a) and relative error (b) between Aeolus detection data and L-band RS data. The
180 **data come from the Rayleigh-clear group for 12 months in the Chifeng.**
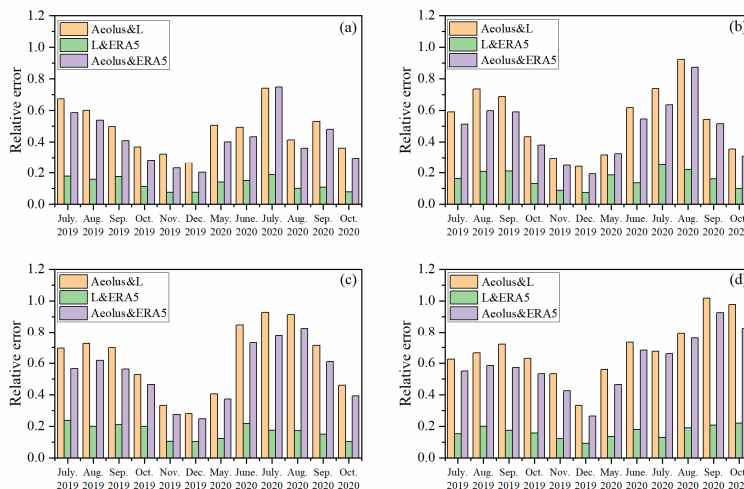
Figure 6. The monthly mean values of the three groups of relative errors in different regions and different months, (a) Chifeng, (b) Baoshan, (c) Shapingba, (d) Qingyuan.

Further, we use Eq. (7) to calculate the monthly average relative error of each month in each region, and then use Eq. (8) to
185 calculate the monthly average of Aeolus relative error parameters. Finally, we obtain the changes of the three sets of relative errors (Aeolus&L, L&ERA5, Aeolus&ERA5) from July 2019 to October 2020 (data missing from January to April 2020), as shown in Fig.6. For the Rayleigh-clear data, the relative error of the Aeolus data is significantly larger in summer. Although the $\bar{D}_r(L\&ERA5)$, which represents the error caused by imperfect space-time matching, also increases in summer, the increase of $\bar{D}_r(Aeolus\&L)$ and $\bar{D}_r(Aeolus\&ERA5)$ in summer months is much larger than that of $\bar{D}_r(L\&ERA5)$. Therefore, we
190 believe that this increase in relative error is caused by the variation in Aeolus detection performance. Meanwhile, the same seasonal trend of Rayleigh-clear data in the four regions (Fig.7a) also confirms this idea as the mean relative error parameter in July is over 174% higher than that in December. In addition, we also found that as the latitude decreases, the month in which the relative error peak appears is delayed. In the two years (2019-2020), the peaks of relative error in Chifeng were in July, while Baoshan and Shapingba were in August and Qingyuan is postponed to September. Meanwhile, the relative errors in the
195 summer of 2020 have increased to varying degrees compared to 2019. This may be related to the differences in summer weather conditions in different years or the decrease in laser power of Aeolus. It is not yet clear.

In addition, we also calculated the monthly average value of D_{Aeolus} in the Mie-cloudy group, as shown in Fig. 7b. The monthly mean value of D_{Aeolus} in the Mie-cloudy group do not show a significant seasonal trend like the Rayleigh-clear group. The

mean relative error parameter in July is only 39% higher than that in December. Its seasonal fluctuations are relatively random

200   for different regions, but the summer relative error is slightly larger overall.
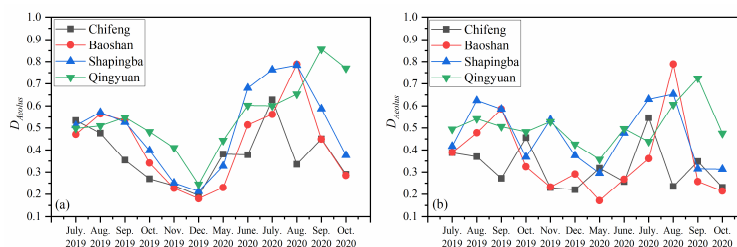
Figure 7. Changes in the monthly average of D_{Aeolus} in different months, (a)Rayleigh-clear, (b)Mie-cloudy.

ECMWF proposed that varying temperature gradients across the instrument's mirror M1 caused seasonal fluctuations in the

quality of Aeolus detection data (Rennie and Isaksen, 2020). After application of corrections for the mirror effects, the seasonal

205   variation caused by the thermal structure of the system itself theoretically become really small. On the other hand, the different

situation of the Mie-cloudy group and the Rayleigh-clear group does not seem to support the explanation that the Aeolus

system itself causes seasonal changes in detection performance.

Considering the difference in detection range between the Rayleigh-clear group and the Mie-cloudy group (Mie-cloudy mainly

detects the aerosol layer), we believe that this seasonal difference may be caused by seasonal changes in the real atmospheric

210   environment. Therefore, we put forward and verified two conjectures based on Aeolus working principle.

3.2.1 Seasonal variations in atmospheric wind direction

Since Aeolus detects only a single line-of-sight wind vector, the detection wind vector is a component of the real wind vector.

Obviously, when the angle between the detection wind vector and the real wind vector approaches 90 °, the real wind vector

has almost no contribution to the detection wind vector, and the detection error is the largest. The closer the angle between the

215   two is to 0° or 180°, the smaller the detection error.

The wind direction of the atmospheric wind field has an obvious seasonal trend. In China, the northwest monsoon prevails in

winter while the southeast in summer. To verify whether the seasonal variation in wind direction is the cause of the seasonal

variation in Aeolus detection performance, we analyse the statistical distribution of the angle between the real horizontal wind

direction and the Aeolus HLOS direction.
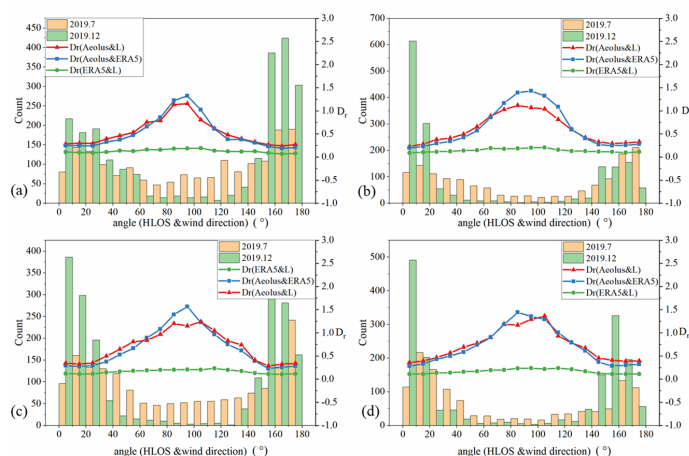
220

Figure 8. The statistical distribution in different angle (HLOS & wind direction) about data points and mean relative errors. The relative error Dr in the figure is calculated from the 12-month data of the region; (a) Chifeng, (b) Baoshan, (c) Shapingba, (d) Qingyuan.

Based on the previous data matching work, we calculate the angle α between the real horizontal wind direction (provided by
225 ERA5 data) and the Aeolus HLOS direction (provided by L2B data) of each Aeolus valid data point. Figure 8 is obtained from
the Rayleigh-clear group data. When the angle α is in the range of 70 °–110 °, the relative error of the Aeolus data increases
significantly. The proportion of data points whose angle is in the range of 70 °–110 ° in July is 8.14% higher than that in
December. Most of the data points in December are concentrated in the vicinity of 0° and 180°. Theoretically, this will
significantly increase the average relative error of Aeolus in July, which may be one of the reasons for the increase in the
230 relative error of Aeolus in summer. For Mie-cloudy group (Fig.9), the proportion of data points whose angle is in the range of
70 °–110 ° in July is 5.86% higher than that in December, which means the same order of magnitude for the angle distribution
difference of Rayleigh-clear data and Mie-cloudy data. However, it is known that the seasonal variation of relative error in the
Mie-cloudy group is much smaller than that in the Rayleigh-clear group, so this conjecture can not explain the seasonal
performance of the Mie-cloudy group.
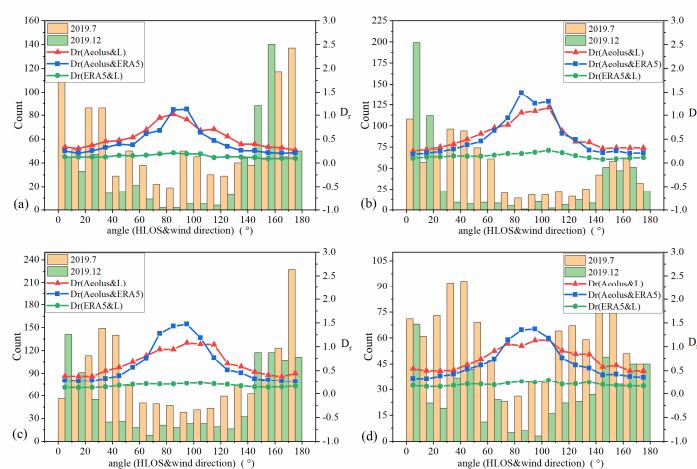
235

Figure 9. Same as Figure 8, but for Mie-cloudy group.

3.2.2 Seasonal variations in upper cloud cover

In the actual work process, the spaceborne wind lidar is susceptible to the influence of cloud-aerosol. When the laser passes
through the cloud-aerosol layer, it will be subject to a strong attenuation effect, resulting in decrease in the energy of the laser
240 beam and signal-to-noise ratio (SNR). At the same time, for the Rayleigh channel, the cloud-aerosol layer will also bring strong
Mie scattering, which will pollute the signal of the Rayleigh channel and increase its detection error (Rennie et al., 2020).
Because the Rayleigh channel has comprehensive coverage in altitude, we takes the effective data of the Rayleigh channel
(both of Rayleigh-clear and Rayleigh-cloudy) and counts the number of samples (N_{clear}, N_{cloudy}) according to the month and
altitude, then defines the parameter r that represents the backscatter ratio:

245
$$r = \frac{N_{clear} + N_{cloudy}}{N_{clear}},$$
(9)

r is normalized to obtain the parameter R. The larger the value of the parameter R, the stronger the scattering of Mie in the
altitude layer. We calculate the R value of 12 months in different regions with a height resolution of 1000 m to get Fig. 10.
Obvious high-altitude Mie scattering layers are existed for the four areas in summer, and in autumn and winter, this Mie
scattering layer moves to areas with lower altitudes with its Mie scattering intensity weakened. In the Qingyuan shown in Fig.
250 10(d), the high-altitude Mie scattering layer in November and December 2019 is very weak.
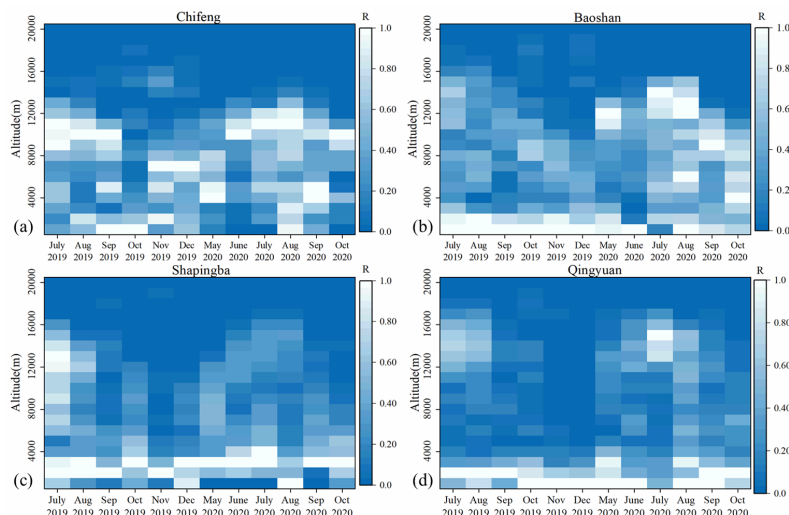
Figure 10. The vertical distribution of R values in different regions and different months. (a) Chifeng, (b) Baoshan, (c) Shapingba, (d) Qingyuan.

The ERA5 cloud coverage information matched with Aeolus data points are showed in Figure 11. The r value in the Fig. 11
is a parameter that represents the backscattering ratio defined by Eq. (9). The mean value of cloud coverage and the value of
r have a similar trend in the vertical direction, but they are different in the near-ground area because the main reason for the
Mie scattering here is aerosols rather than clouds. Taken together, the high-altitude Mie scattering layer in Fig.10 in summer
is caused by the presence of clouds in this area.
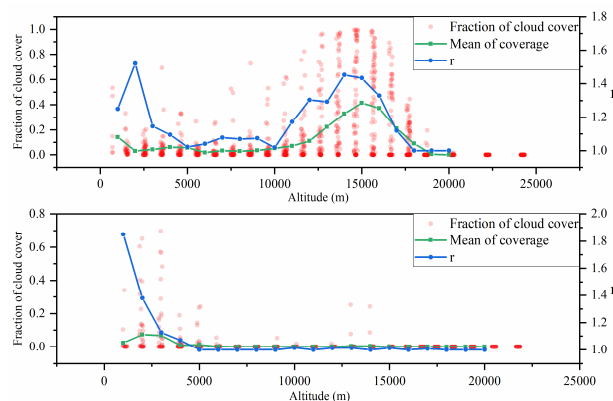
Figure 11. The ERA5 cloud coverage of the valid Rayleigh channel data in the vertical direction. The above picture is the data of Qingyuan in July 2019, and the picture below is the data of Qingyuan in December 2019. The green line is the mean value of cloud coverage at different distance gates.

In other words, the height of cloud tops in summer increases significantly within the Aeolus detection height
range. Combining the results of the two figures (Fig. 10 and Fig. 11), the cloud top height in July is about 3-5km
higher than that in December for four regions, which is consistent with the seasonal variation rule of cloud top
height in East Asia (Zhao et al., 2020).

When the satellite-borne wind lidar works, high-altitude cloud layer will inevitably attenuate the laser beam and
reduce the energy of the laser beam passing through the cloud layer. As a result, the SNR of the echo signal in
the area below the high cloud decreases and the detection error increases. At the same time, the Rayleigh signal
from the cloudy area will be interfered by the Mie scattering signal, which will affect the calculation of its
Doppler shift. Although the Aeolus data processing algorithm uses a strict backscatter ratio threshold to remove

the Rayleigh channel data elements that may contain Mie scattering from the Rayleigh-clear group (Rennie et al., 2020), the signal interference still affects the final inversion result.

Finally, we try to use this conjecture to explain why the Mie-cloudy group's relative error seasonal variation are not obvious (Fig. 7b). There are two special data points in Fig.7b that are July and August 2020 in Baoshan. They are all summer, but the average relative error in August is significantly higher than that in July. The vertical distribution about the valid data points and all data points of the Mie-cloudy group in the two months are showed in Fig. 12. The data points in July are mainly distributed in the high-altitude cloud area. It may be due to the dense clouds in the upper air in July, and it is difficult for Mie channel to detect the area below the clouds. The high-altitude cloud layer's Mie scattering signal closing to the satellite, which means the small optical thickness and the high SNR, improves the Aeolus data quality. In addition, the Mie channel discriminator is not sensitive to the Rayleigh scattering signal, so there is unnecessary to consider the Rayleigh signal interference (Rennie et al., 2020). In August, the data points are evenly distributed in the vertical direction, and the amount of low-altitude data still accounts for a considerable proportion. Before the laser beam reaches low altitude, it is attenuated by high-altitude clouds. The low-altitude Mie scattered echo signal generated by the laser beam propagates through the upper atmosphere and attenuate again. This means that it will become very weak when it reaches the Aeolus receiving telescope, which is not conducive to subsequent signal processing and reduces the quality of the Mie-cloudy data. When we use D_{Aeolus} to represent the value of SNR, as shown in Fig. 12, D_{Aeolus} is significantly higher in August than that in July when the altitude is lower than 8km, which supports the above explanation. That is to say, in summer, a considerable part of the data in the Mie-cloudy group comes from high altitude, but the low-altitude Mie scattering signal and the high-altitude Mie scattering signal contribute to the overall relative error in the opposite way. This may be the reason why the seasonal variation of Aeolus relative error in the Mie-cloudy group is not obvious.
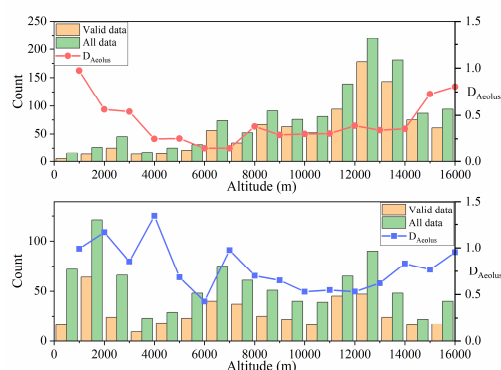
Figure 12. Distribution of Mie-cloudy data points and D_{Aeolus} in altitude. (a) July 2020, (b) August 2020, and data are all from Baoshan.

4 Conclusion

In this study, the seasonal variation of Aeolus detection performance in China is analyzed by using Aeolus detection data, L-band RS detection data and ERA5 data from July 2019 to December 2019 and may 2020 to October 2020.

Firstly, the difference between Aeolus data and L-band RS data is discussed, and the selection threshold of Aeolus data estimation error is clarified, which is 8m/s for the Rayleigh-clear data and 4m/s for the Mie-cloudy data. After the valid data filtered, a comparative analysis of the three wind field data is carried out. The R value of Aeolus' Rayleigh-clear (Mie-cloudy) data and ERA5 data is 0.95 (0.97), and the R value of L-band RS data is 0.92 (0.94). This shows that the Aeolus detection data is in good agreement with the ERA5 and L-band RS data, and quality of the data used in this paper is reliable.

Then these three data sets are used to calculate the monthly mean value of relative error. From the calculation results, the relative errors of the Rayleigh-clear data increase significantly for the four regions in the summer as the mean relative error parameter in July is 174% higher than that in December. In the Mie-cloudy group, this seasonal trend is not obvious and the performance is more random. Combining the working principle of Aeolus, we propose two conjectures to explain the seasonal variation of the relative error of Aeolus data. One is the variation in the angle between the actual horizontal wind direction and Aeolus HLOS direction, which may affect the extent of Aeolus single vector data to reflect the true wind vector. The other is the seasonal variation of the altitude of the high-altitude clouds and cloud tops, which may affect the SNR of the echo signals in different channels.

For the first conjecture, we calculates the distribution of the angle between the actual horizontal wind direction and Aeolus HLOS direction of different regions in July and December. It is found that there were obviously more data points distributed in the high error interval of 70°–110° in July than December, which proved that this conjecture is reasonable. However, the first conjecture encounters problems in explaining the situation of the Mie-cloudy data. For the second conjecture, we sets the parameter R to represent the backscattering ratio, and calculates the distribution of R at different altitudes in different months. It is found that there is a strong high-altitude Mie scattering layer in summer. Combining with cloud coverage information, we know that the Mie scattering layer is caused by high-altitude clouds in summer. The high-altitude clouds reduce the signal-to-noise ratio of the echo signal received by Aeolus, and also interfere with the signal analysis and processing of the Rayleigh channel. This conjecture is also reasonable and can reasonably explain the seasonal variation in the relative error of the Mie-cloudy channel Aeolus.

In this study, the analysis of the Aeolus data quality and its seasonal changes in the four regions (Chifeng, Baoshan, Shapingba and Qingyuan) of China will help to better understand and use the Aeolus detection data over China. Besides, as the first spaceborne wind lidar, the analysis of factors affecting the detection performance of Aeolus will help provide a reference for the follow-up development of spaceborne wind lidar.

Data availability

The Aeolus L2B data used in this paper can be downloaded from https://aeolus-ds.eo.esa.int/oads/access/collection (last accessed 13 March 2021). The L-band RS data can be provided for non-commercial research purpose upon request (Yinchao Zhang: ychang@bit.edu.cn). The ERA5 data can be downloaded from https://cds.climate.copernicus.eu/cdsapp#!/dataset/10.24381/cds.bd0915c6?tab=overview (last accessed 13 March 2021).

Author contributions

S. Chen and R. Cao conceived of the idea for verified the seasonal variation of Aeolus detection performance over China; R. Cao and Y. Xie conducted the data analyses and co-wrote the manuscript; Y. Zhang, W. Tan, H. Chen, P. Guo and P. Zhao discussed the experimental results. All coauthors helped reviewing the manuscript.

Competing interests

The authors declare that they have no conflict of interest.

Acknowledgements

We are very grateful to the China Meteorological Administration for the L-band RS data in China, to ESA for the Aeolus data and to ECMWF for ERA5.

References

340 Baars, H., Herzog, A., Heese, B., Ohneiser, K., Hanbuch, K., Hofer, J., Yin, Z., Engelmann, R., and Wandinger, U.: Validation of Aeolus wind products above the Atlantic Ocean, Atmospheric Meas. Tech., 13, 6007–6024, https://doi.org/10.5194/amt-13-6007-2020, 2020.

Belova, E., Kirkwood, S., Voelger, P., Chatterjee, S., Satheesan, K., Hagelin, S., Lindskog, M., and Körnich, H.: Validation of Aeolus winds using ground-based radars in Antarctica and in northern Sweden, Atmospheric Meas. Tech. Discuss., 1–19, 345 https://doi.org/10.5194/amt-2021-54, 2021.

European Space Agency, Andersson, E., and Clissold, P. (Eds.): ADM-Aeolus: science report, ESA Communication Production Office, Noordwijk, Netherlands, 121 pp., 2008.

Frehlich, R.: Estimation of velocity error for Doppler lidar measurements, J. Atmospheric Ocean. Technol., 18, 1628–1639, 2001.

350 Guo, J., Miao, Y., Zhang, Y., Liu, H., Li, Z., Zhang, W., He, J., Lou, M., Yan, Y., and Bian, L.: The climatology of planetary boundary layer height in China derived from radiosonde and reanalysis data, Atmospheric Chem. Phys., 16, 13309–13319, 2016.

Guo, J., Liu, B., Gong, W., Shi, L., Zhang, Y., Ma, Y., Zhang, J., Chen, T., Bai, K., Stoffelen, A., de Leeuw, G., and Xu, X.: Technical note: First comparison of wind observations from ESA's satellite mission Aeolus and ground-based radar wind 355 profiler network of China, Atmospheric Chem. Phys., 21, 2945–2958, https://doi.org/10.5194/acp-21-2945-2021, 2021.

Hauchecorne, A., Khaykin, S., Wing, R., Mariscal, J.-F., Porteneuve, J., Cammas, J.-P., Marquestaut, N., Payen, G., and Duflot, V.: Validation of ESA Aeolus wind observations using French ground-based Rayleigh Doppler lidars at midlatitude and tropical sites, 22, 19786, 2020.

Hersbach, H., Bell, B., Berrisford, P., Hirahara, S., Horányi, A., Muñoz-Sabater, J., Nicolas, J., Peubey, C., Radu, R., and 360 Schepers, D.: The ERA5 global reanalysis, Q. J. R. Meteorol. Soc., 146, 1999–2049, 2020.

Ishii, S., Okamoto, K., Baron, P., Ishibashi, T., Tanaka, T., Sekiyama, T., Maki, T., Kubota, T., Satoh, Y., Sakaizawa, D., Yamashita, K., Gamo, K., Ochiai, S., Yasui, M., Oki, R., Satoh, M., and Iwasaki, T.: Study on measurement performance of future space-based Doppler wind lidar in Japan, in: 2017 IEEE International Geoscience and Remote Sensing Symposium (IGARSS), 2017 IEEE International Geoscience and Remote Sensing Symposium (IGARSS), 4238–4245, 365 https://doi.org/10.1109/IGARSS.2017.8127938, 2017.

Liu, B., Guo, J., Gong, W., Zhang, Y., Shi, L., Ma, Y., Li, J., Guo, X., Stoffelen, A., de Leeuw, G., and Xu, X.: Intercomparison of wind observations from ESA's satellite mission Aeolus, ERA5 reanalysis and radiosonde over China, Atmospheric Chem. Phys. Discuss., 1–35, https://doi.org/10.5194/acp-2021-41, 2021.

Lux, O., Lemmerz, C., Weiler, F., Marksteiner, U., Witschas, B., Rahm, S., Geiß, A., and Reitebuch, O.: Intercomparison of 370 wind observations from the European Space Agency's Aeolus satellite mission and the ALADIN Airborne Demonstrator, Atmospheric Meas. Tech., 13, 2075–2097, https://doi.org/10.5194/amt-13-2075-2020, 2020.

Martin, A., Weissmann, M., Reitebuch, O., Rennie, M., Geiß, A., and Cress, A.: Validation of Aeolus winds using radiosonde observations and numerical weather prediction model equivalents, Atmospheric Meas. Tech., 14, 2167–2183, https://doi.org/10.5194/amt-14-2167-2021, 2021.

375 Reitebuch, O.: The Spaceborne Wind Lidar Mission ADM-Aeolus, in: Atmospheric Physics: Background – Methods – Trends, edited by: Schumann, U., Springer, Berlin, Heidelberg, 815–827, https://doi.org/10.1007/978-3-642-30183-4_49, 2012.

Reitebuch, O., Lemmerz, C., Lux, O., Marksteiner, U., Rahm, S., Weiler, F., Witschas, B., Meringer, M., Schmidt, K., Huber, D., Nikolaus, I., Geiss, A., Vaughan, M., Dabas, A., Flament, T., Stieglitz, H., Isaksen, L., Rennie, M., de Kloe, J., Marseille, G.-J., Stoffelen, A., Wernham, D., Kanitz, T., Straume, A.-G., Fehr, T., von Bismarck, J., Floberghagen, R., and Parrinello, 380 T.: Initial Assessment of the Performance of the First Wind Lidar in Space on Aeolus, in: EPJ Web of Conferences, ILRC29, Heifei, China, 1–4, 2019.

Rennie, M. and Isaksen, L.: Aeolus L2B status, monitoring and NWP impact assessment at ECWMF, in: Aeolus NWP Impact Assessment Workshop, Darmstadt, Germany, 2019.

Rennie, M. and Isaksen, L.: The NWP impact of Aeolus Level-2B winds at ECMWF, ECMWF Technical Memo 864, Shinfield 385 Park, Reading, UK, https://doi. org/10 …, 2020.

Rennie, M., Tan, D., Andersson, E., Poli, P., and Dabas, A.: (MATHEMATICAL DESCRIPTION OF THE AEOLUS LEVEL-2B PROCESSOR), 124, 2020.

Shin, H., Ahn, M.-H., Kim, J., and Chung, C.-Y.: Aeolus / ALADIN data analysis in Korea, 22, 19595, 2020.

390   Stoffelen, A., Pailleux, J., Källén, E., Vaughan, J. M., Isaksen, L., Flamant, P., Wergen, W., Andersson, E., Schyberg, H., Culoma, A., Meynart, R., Endemann, M., and Ingmann, P.: THE ATMOSPHERIC DYNAMICS MISSION FOR GLOBAL WIND FIELD MEASUREMENT, Bull. Am. Meteorol. Soc., 86, 73–88, https://doi.org/10.1175/BAMS-86-1-73, 2005.

Witschas, B., Lemmerz, C., Geiß, A., Lux, O., Marksteiner, U., Rahm, S., Reitebuch, O., and Weiler, F.: First validation of Aeolus wind observations by airborne Doppler wind lidar measurements, Atmospheric Meas. Tech., 13, 2381–2396, https://doi.org/10.5194/amt-13-2381-2020, 2020.

395   Zhang, C., Sun, X., Lu, W., Shi, Y., Dou, N., and Li, S.: On the relationship between wind observation accuracy and the ascending node of sun-synchronous orbit for the Aeolus-type spaceborne Doppler wind lidar, Atmospheric Meas. Tech. Discuss., 1–23, https://doi.org/10.5194/amt-2020-202, 2020.

Zhao, M., Zhang, H., Wang, H.-B., Zhou, X.-X., Zhu, L., An, Q., and Chen, Q.: The change of cloud top height over East Asia during 2000–2018, Adv. Clim. Change Res., 11, 110–117, https://doi.org/10.1016/j.accre.2020.05.004, 2020.

400